Available online at www.sciencedirect.com
SCIENCE DIRECT®
International Journal of Multiphase Flow 30 (2004) 779–801
International Journal of Multiphase Flow
www.elsevier.com/locate/ijmulflow

Interfacial structures and interfacial area transport in downward two-phase bubbly flow ☆

M. Ishii *, S.S. Paranjape, S. Kim, X. Sun

School of Nuclear Engineering, Purdue University, 400 Central Drive, West Lafayette, IN 47907-1290, USA

Received 19 October 2003; received in revised form 14 April 2004

Abstract

An adiabatic, air–water, co-current, vertically downward bubbly flow was studied to gain a better understanding of interfacial structures and flow characteristics. The experimental test sections were round pipes with internal diameters of 25.4 and 50.8 mm. Flow regime map was obtained using characteristic signals obtained from an impedance void meter, and a neural network-based identification methodology to minimize the subjective judgment in determining the flow regimes. A four-sensor conductivity probe was used to measure the local two-phase flow parameters that characterize the interfacial structures. The parameters measured were: void fraction, interfacial area concentration, bubble velocity, and bubble Sauter mean diameter. Furthermore, a laser Doppler anemometer (LDA) system was used to measure local axial liquid velocity and turbulence. The local profiles of these parameters as well as their axial development revealed the nature of the interfacial structures and the bubble interaction mechanisms occurring in the flow. Based on previous study of interfacial area transport for upward flows, the interfacial area transport equation applicable to downward flow was developed with certain modifications in bubble interaction terms.

Keywords: Downward flow; Interfacial area concentration; Interfacial area transport equation; Four-sensor conductivity probe; Two-phase flow

☆ It is our great pleasure to celebrate Professor George Yadigaroglu's 65th birthday and his many years of great contributions to the field of multiphase flow and heat transfer. Our exchanges of ideas and collaborations in research started very early during our Ph.D. student time since both of us worked on the density wave instabilities. We are fascinated to find out that Professor Yadigaroglu experimentally found the higher order density wave instabilities at MIT that was theoretically predicted by a model developed by us at Georgia Tech at one of the national heat transfer conference. On this occasion we would like to congratulate him for his great accomplishments and wonderful leadership in the nuclear thermal-hydraulics.

* Corresponding author. Tel.: +1-765-494-4587; fax: +1-765-494-9570.
E-mail address: ishii@ecn.purdue.edu (M. Ishii).

0301-9322/$ - see front matter © 2004 Elsevier Ltd. All rights reserved.
doi:10.1016/j.ijmultiphaseflow.2004.04.009

1. Introduction

The study of downward two-phase flow is important in view of nuclear reactor safety analysis and industrial energy transfer systems. In particular, downward two-phase flow could occur in light water reactor (LWR) accidents including the loss of coolant accident (LOCA) and loss of heat sink accident (LOHS) due to feed water loss or secondary loop pipe break. In such scenarios, co-current downward two-phase flow may occur in the steam generator. It is also possible that the two-phase flow may go through upflow, counter-current flow and down flow in cases of small break LOCA or safety relief valve open. In a boiling water reactor (BWR), the co-current downward two-phase flow can be encountered in the later stages of the emergency core cooling system (ECCS) injection, at the top of the core and it may also lead to the counter-current flow limitation phenomena.

For accurate prediction of the transient phenomena occurring in a reactor system or other two-phase flow systems, two-fluid model is used in safety system analysis codes. Since the two-fluid model treats each phase separately, interfacial transfer terms appear in the governing equations. To correctly model these interfacial transfer terms, there is a need to clearly understand the interfacial structures and to specify the interfacial area concentration. There exists a great deal of literature on flow regime transitions in upward, downward as well as counter-current two-phase flows (Taitel et al., 1980; Mishima and Ishii, 1984; Taitel and Barnea, 1983; Barnea, 1987; Crawford et al., 1985). In particular, flow regimes have also been studied for bottom-reflooding of vertical tubes under constant and oscillatory injection rates (Yadigaroglu, 1983; Kawaji et al., 1985). While interfacial structures have been studied by many researchers in upward two-phase flows, relatively little attention has been paid to the downward two-phase flows. Most of the previous research focused mainly on the flow regime identification by flow visualization method (Oshinowo and Charles, 1974; Barnea et al., 1982; Yamaguchi and Yamazaki, 1984; Usui and Sato, 1989). These studies as well as the recent results from the downward two-phase flow experiments demonstrated that the interfacial structures in downward two-phase flows are quite different from those in upward two-phase flows (Goda, 2001; Paranjape, 2003). In the current experiments, an objective method based on neural network classification methodology was used for the identification of the flow regimes. The local interfacial structures were studied for downward two-phase bubbly flow using a four-sensor conductivity probe and a laser Doppler anemometry (LDA) system. Finally, the interfacial area transport model was evaluated using the area-averaged data.

2. Experimental facility

The experimental loop was an adiabatic vertical air–water system. The schematic diagram of the experimental loop is shown in Fig. 1. The two test sections were made of round acrylic pipes of 25.4 and 50.8 mm internal diameters (ID). The total length of each test section was 3810 mm corresponding to $L/D = 150$ and 75 for 25.4 and 50.8 mm ID pipes, respectively. Water was supplied by a 25 hp centrifugal pump and controlled by a combination of a frequency converter and valves. The water flow rate was measured by an electro-magnetic flow meter, with an accuracy of $\pm 3\%$ when the flow rate is more than 50% of the full scale. Air was supplied via external

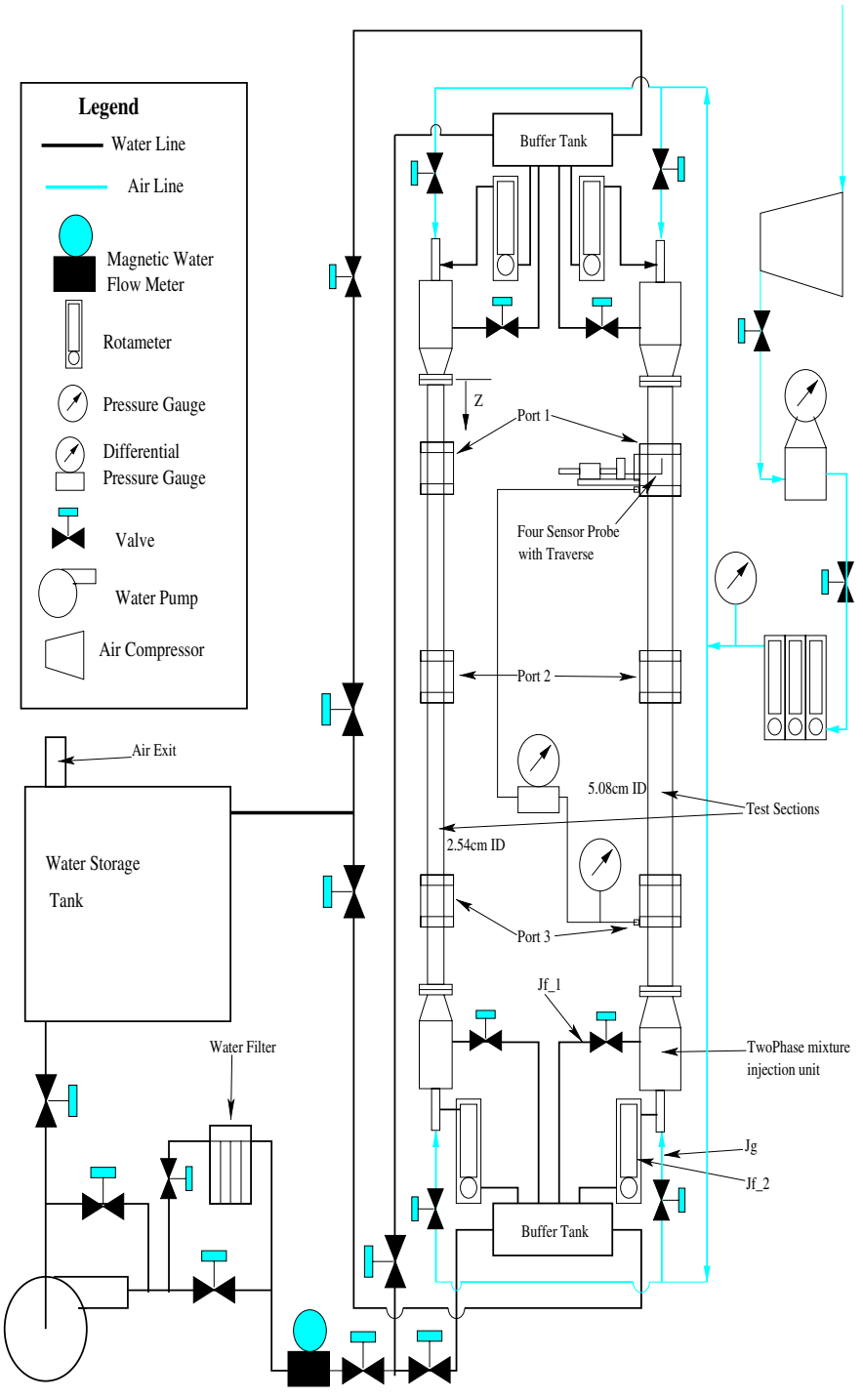

Fig. 1. Schematic diagram of the experimental setup.

compressors with pressure maintained by a pressure regulator at 690 kPa (100 psia). The gas flow rate was measured by several rotameters with an accuracy of ±3% when the flow rate is more than 50% of the full scale. Water was injected into an air–water mixture injection unit where a bubble generator was located. A sparger with an average pore size of 10 μm was employed as the bubble generator, which produces near uniform bubbles of approximately 1–2 mm in diameter at the inlet of the test section. The air–water mixture injection unit was employed at both the top and the bottom of each test section so that the loop was capable of operating in both upward and downward flow configurations.

An impedance meter was employed to obtain the area-averaged void signals. The impedance void meter is a non-intrusive conductance type probe that utilizes the difference in the electrical conductivity between air and water. A pair of stainless steel plates were employed as the electrodes, and they were flush mounted against the inner wall of the test section. The electrodes span 90° of the cross section with a thickness of 0.953 cm. The thickness was chosen so as to be larger than the dimension of a typical spherical bubble, yet shorter than the length of a typical cap or a slug bubble. The impedance signals from the impedance meter were employed for the flow regime identification study, as well as for the area-averaged void fraction data.

The four-sensor conductivity probe was used to acquire the local two-phase flow parameters. The raw signal obtained from the probe was fed to a signal processing program, which calculated the local parameters from the raw data. The measurement principles of the four-sensor conductivity probe are presented by Revankar and Ishii (1993) and Kim et al. (2000a) . These local parameters included void fraction (ϵ), interfacial area concentration (a_i), and bubble velocity (v_G). These parameters were measured at three axial locations in each test section. In the 25.4 mm ID test section, the local parameters were measured at $z/D = 13$, 68 and 133, while in the 50.8 mm ID test section, the measurements were taken at $z/D = 7$, 34 and 67. Here, z is the axial distance from the inlet of the test section and D is the inner diameter of the test section. At each axial measurement location, the probe was traversed in the radial direction to take measurements at different r/R locations, namely, $r/R = 0$, 0.2, 0.4, 0.5, 0.6, 0.7, 0.8 and 0.9, where r is the radial distance from the center line of the pipe and R is the inner radius of the pipe. The spacing between the measurement points was chosen such that it is coarser near the center of the pipe and finer near the wall of the pipe, considering the fact that the variation of the local two-phase flow parameters may be higher near the pipe wall and the near wall values have more impact on the area-averaged quantities. The area-averaged parameters were calculated from the local parameters, by integrating them over the pipe cross section, assuming radial symmetry. The measurement error of the present probe is estimated to be less than ±7% (Kim et al., 2000b).

For preliminary classification, the measured chord lengths were used and bubble signals were grouped into group 1 and group 2 using the criteria for the boundary between distorted and cap bubbles. Here, the boundary between group 1 and group 2 bubbles was taken as the maximum stable diameter of distorted bubbles (Ishii and Zuber, 1979),

$$D_{d,max} = 4\sqrt{\frac{\sigma}{g\Delta\rho}}. \tag{1}$$

It was necessary to introduce two groups based on the difference in the bubble interaction mechanisms for these groups of the bubbles. To have the statistical error within ±10% of the measured values at each location, the data acquisition time was adjusted such that at least 2000

bubbles were encountered by the probe tip (Wu and Ishii, 1999). To assess the accuracy of the probe measurement, the area-averaged value of the product of the local void fraction and the local gas velocity, $\langle \epsilon v_G \rangle$, was compared with the superficial gas velocity, $\langle j_G \rangle$, obtained from the measurement of volumetric gas flow rate and local pressure. It was observed that the two values agreed well within the experimental measurement error of ±10% for most of the flow conditions.

An integrated LDA system from TSI Inc., was used in the present experiment for measurement of local axial liquid velocity and turbulence. The system included an argon-ion laser, a multicolor beam separator, a multicolor receiver, a signal processor, a fiber-optic probe, an IBM PC and a postprocessing software. The system was capable of one-dimensional velocity measurement. Back-scattering was the available mode to receive scattered light. The argon-ion laser had a maximum power of 100 mW. The LDA measurement was performed at an axial location of $z/D = 52.5$ in 50.8 mm ID test section. The measurement volume was traversed in 2.5 mm increments in the regions of $r/R < 0.7$ and then in 1.25 mm increments in the region near the wall. The measurement volume had a diameter of 90.5 μm and a length of 1.31 mm. Titanium dioxide particles having a mean size of 2 μm were used as seeding particles, which served as scattering media for the laser beams. The negligible effects of the seeding particles on the two-phase flow characteristics were confirmed by the four-sensor conductivity probes by running the test with and without seeding particles and comparing the local time averaged quantities for void fraction and interfacial area concentration.

The application of LDA in gas–liquid two-phase flow becomes complicated as the large particles such as bubbles also scatter or reflect the laser light; and the burst signals generated by these scattered lights may also be interpreted as effective velocity signals by the LDA system. Hence it may be necessary to distinguish the signals coming from the seeding particles and the bubble interfaces depending on the flow conditions. In view of this, significant efforts have been made by many researchers to distinguish the liquid phase signals from those in the bubble interfaces (Durst and Zare, 1975; Theofanous and Sullivan, 1982; Tsuji and Morikawa, 1982; Marie and Lance, 1983; Ohba et al., 1986; Velidandla et al., 1996). In the LDA experiment, the measurements were performed in relatively low void fraction conditions. The maximum area-averaged void fraction was about 8.5%. The ratio of the number density of seeding particles to that of bubbles was on the order of 100 or higher. Furthermore, a high voltage was applied to the photo-multiplier tube (PMT) of the LDA system at around 1100 V. These procedures ensured that the relative contribution from the bubble interfaces to all effective burst signals became statistically insignificant compared to those from the seeding particles. Hence, no further processing of data was needed to distinguish the liquid velocity signals from the bubble interface signals at these flow conditions. The mean axial velocity and its fluctuation were directly obtained from the LDA without any further data reduction or discrimination.

3. Experimental results

3.1. Flow regime identification

An impedance void meter is capable of acquiring the near instantaneous area-averaged signals that represent the structural characteristics of the flow which is strongly related to the void

fraction. For this reason, the signals obtained by the impedance void meter can be utilized as a discriminator for the flow regime identification. From the visual observation of the signals and the probability density functions and power spectral density functions of the impedance signals it was considered that various statistical moments of the impedance signal would reflect the characteristics of the flow regimes. A self-organizing neural network classification technique was utilized in order to determine the flow regime from the impedance signals (Mi et al., 2001). The mean, standard deviation, and skewness derived from the impedance signals were adopted to train the neural network in this investigation. These three statistical parameters derived from the impedance signals were fed into a self-organizing neural network as an input matrix. The neural network trained by these input parameters, classified them into four categories. The classification categories adopted in this investigation correspond to four flow regimes, which were observed by flow visualization, viz. bubbly, slug, churn-turbulent, and annular flows.

The resulting flow regime maps for both downward flows in the 25.4 and 50.8 mm ID pipes are shown in Figs. 2 and 3 respectively. It may be noted that in these figures, the flow regime maps are shown in the third quadrant, because upward direction is considered positive in common literature. Unlike the upward two-phase flows, it was found that the flow regime transition in cocurrent downward two-phase flows strongly depended on the flow channel dimension. It is also noted that in the 50.8 mm ID test section, a kinematic shock condition was observed. This shock represented the abrupt transition from bubbly to annular flow regime within the test section. Under this condition, annular flow appeared on the upstream side of the shock and bubbly flow on the downstream region.

3.2. Local data analysis

To study the details of the interfacial structures, fifteen flow conditions were chosen in the bubbly flow regime for the 25.4 mm ID test section and ten flow conditions in the bubbly flow regime for the 50.8 mm ID test section. These flow conditions are shown in Tables 1 and 2,

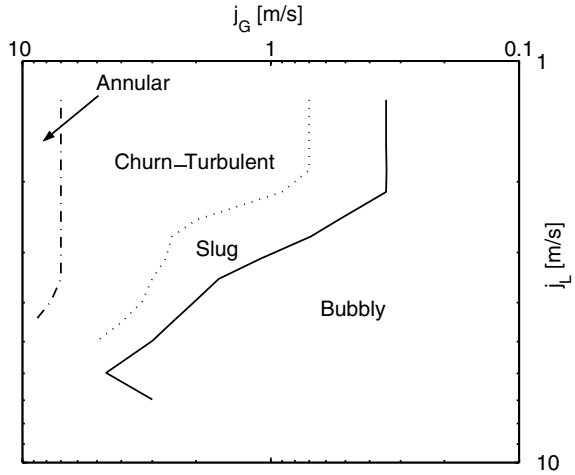

Fig. 2. Flow regime map for 25.4 mm ID test section for downward flow.

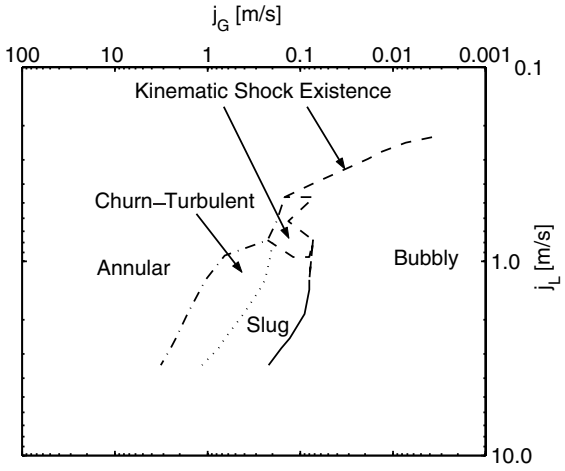

Fig. 3. Flow regime map for 50.8 mm ID test section for downward flow.

Table 1
Flow conditions for 25.4 mm ID test section

Run no.	j_G [m/s]	j_L [m/s]	$\langle\epsilon\rangle$ [–]	$\langle a_i\rangle$ [1/m]
1	0.015	1.250	0.014	41.80
2	0.087	1.250	0.067	158.19
3	0.085	2.120	0.032	69.31
4	0.086	3.110	0.029	72.77
5	0.404	3.110	0.117	251.97
6	0.243	1.250	0.191	249.07
7	0.317	2.120	0.155	166.70
8	0.068	4.000	0.015	43.79
9	0.068	5.070	0.014	51.01
10	0.253	3.970	0.055	147.73
11	0.248	4.980	0.047	189.34
12	0.595	4.030	0.113	292.02
13	0.570	4.960	0.097	332.99
14	1.974	3.990	0.291	449.50
15	1.977	4.970	0.234	538.59

respectively. The local two-phase flow parameters were measured by the four-sensor conductivity probe and the LDA system. The characteristic results from local parameter measurements are presented in this subsection. The local profiles of the two-phase flow parameters at different axial locations revealed the bubble interaction mechanisms.

To highlight the transport characteristics, the results from Runs 2, 8, 7 and 14 in 25.4 mm ID test section and Run 5 from 50.8 mm ID test section are presented. Figs. 4 and 5 show the profiles of the void fraction, interfacial area concentration, and bubble velocity for Run 2 in 25.4 mm ID test section. Figs. 6 and 7 depict the ϵ and a_i profiles for Run 8 in 25.4 mm ID test section and for

Table 2
Flow conditions for 50.8 mm ID test section

Run no.	j_G [m/s]	j_L [m/s]	$\langle\epsilon\rangle$ [–]	$\langle a_i\rangle$ [1/m]
1	0.004	0.620	0.004	10.22
2	0.004	1.250	0.002	3.96
3	0.028	1.250	0.003	27.13
4	0.023	2.490	0.007	12.65
5	0.040	0.620	0.062	112.29
6	0.048	1.260	0.043	83.04
7	0.071	2.490	0.024	31.45
8	0.078	3.480	0.025	44.89
9	0.158	3.470	0.054	87.55
10	0.078	1.250	0.059	59.13

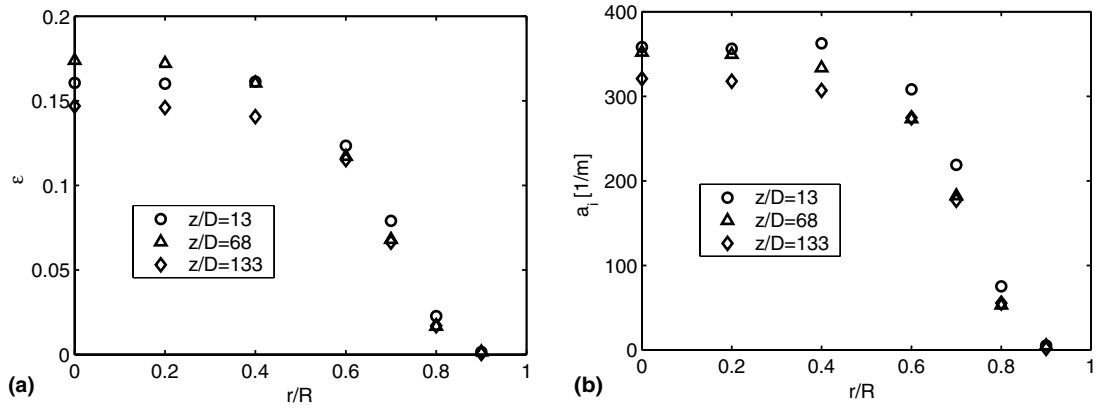

Fig. 4. Local parameter profiles for Run 2 in 25.4 mm ID test section. (a) Void fraction; (b) interfacial area concentration.

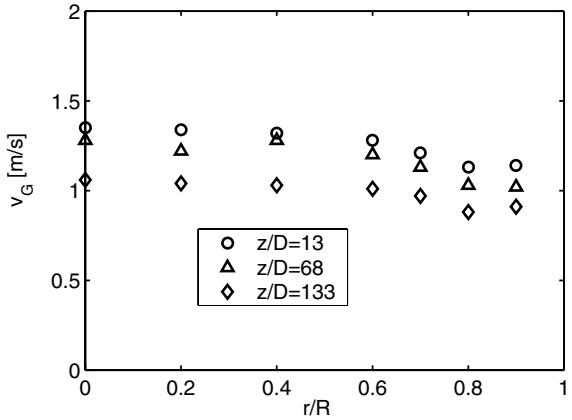

Fig. 5. Bubble velocity profiles for Run 2 in 25.4 mm ID test section.

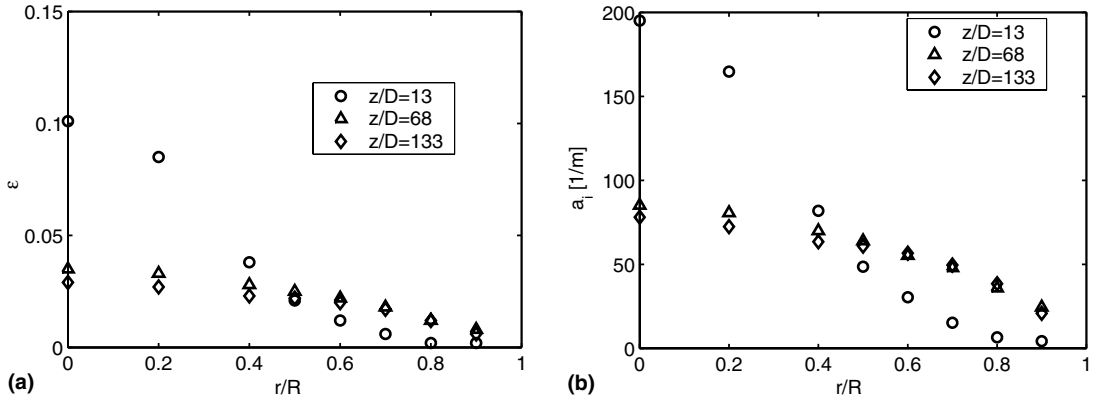

Fig. 6. Local parameter profiles for Run 8 in 25.4 mm ID test section. (a) Void fraction; (b) interfacial area concentration.

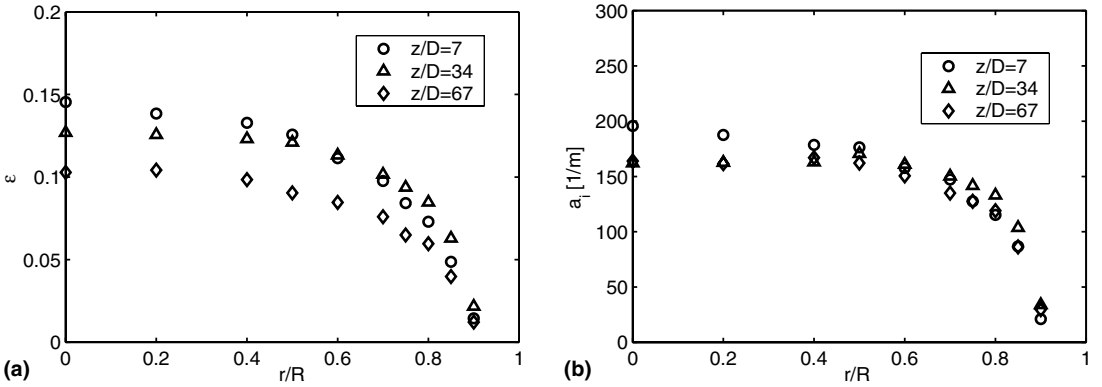

Fig. 7. Local parameter profiles for Run 5 in 50.8 mm ID test section. (a) Void fraction; (b) interfacial area concentration.

Run 5 in 50.8 mm ID test section respectively. In most of the bubbly flow conditions, the void fraction profile peaks at the center of the pipe. This can be explained on the basis of the direction of the lift force acting on the bubbles. In the downward flow, the lift force on the bubbles acts towards the center of the channel. Hence, the bubbles tend to agglomerate in the center of the channel causing increase in the void fraction in the center. This observation is opposite to that in the upward flow, where wall peak can be commonly observed. It is worthwhile to note that in the downward flow, the bubbles move slower than the liquid due to buoyancy force acting in the direction opposite to the direction of the main flow, while the opposite is observed in the upward flow. Since the lift force is proportional to the product of the radial gradient of the axial velocity of the continuous phase and the relative velocity, the direction of the lift force is opposite for upward and downward flows.

Figs. 4(a) and 6(a) show the void profiles of Runs 2 and 8 in the 25.4 mm ID test section, respectively. They have similar superficial gas velocities ($j_G = 0.087$ and 0.068 m/s, respectively)

but different superficial liquid velocities ($j_L = 1.25$ and 4.00 m/s, respectively). It is interesting to note that, while Run 2 shows a flat void profile near the central region, Run 8 shows a strong center peak. It can be speculated that the effect of the lift force may be higher in the flow condition with higher superficial liquid velocity due to larger gradient of axial velocity of the continuous phase in the radial direction. The effect of velocity gradient can also be observed by comparing the void profiles in different diameter test sections. In general it was observed that the void profiles are flatter in the central region of 50.8 mm ID test section as compared to that of 25.4 mm ID test section. However, it is interesting to note that in some flow conditions, the void profiles show off-centered peak, for example, at $z/D = 13$ in Run 2 in the 25.4 mm ID test section (Fig. 4). This off-centered peak distribution of the void fraction is also reported by Wang et al. (1987) and Kashinsky and Randin (1999). This phenomenon of the off-center peaked void distribution needs further investigation.

The interfacial area concentration is proportional to the void fraction and inversely proportional to the bubble Sauter mean diameter. In most of the flow conditions, the radial distribution of the group 1 bubble Sauter mean diameter was uniform. Hence, the radial profiles of void fraction and the interfacial area concentration were quite similar. As the group 2 bubbles are formed, the Sauter mean diameter increases and has a broad peak at the center. The increase in the Sauter mean diameter tends to reduce the interfacial area concentration in the center. Such flow conditions showed dissimilarity in the ϵ and a_i profiles.

Axial bubble velocities are measured by the conductivity probe, while axial liquid velocities and turbulence are measured by the LDA system. The characteristic results from the LDA measurements are presented for Runs 5, 8, 9 and 10 for 50.8 mm ID test section in Figs. 8–11 respectively. In each figure, sub-figure (a) shows the radial profiles of the following quantities:

(1) mean liquid velocity measured by the LDA ($v_{L,2\phi}$);
(2) mean liquid velocity measured by the LDA in single-phase flow having the same superficial liquid velocity ($v_{L,1\phi}$);
(3) estimated liquid velocity ($v_{L,corr}$) from the following correlation (Hibiki et al., 1998),

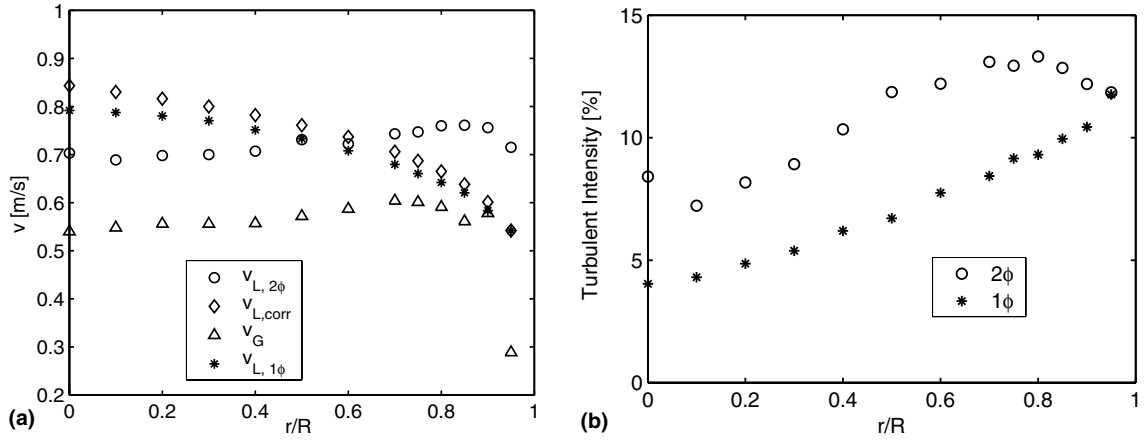

Fig. 8. Mean velocity (a) and turbulent intensity (b) profiles for Run 5 in 50.8 mm ID test section at $z/D = 52.5$.

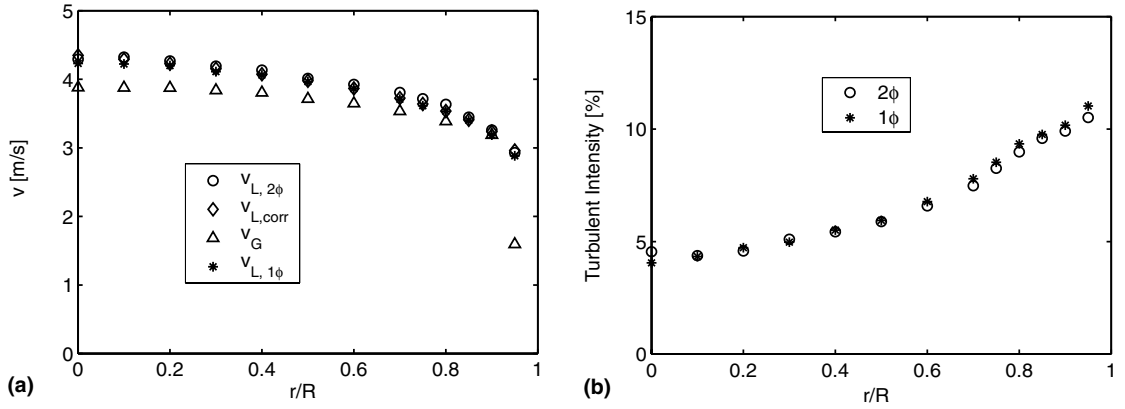

Fig. 9. Mean velocity (a) and turbulent intensity (b) profiles for Run 8 in 50.8 mm ID test section at $z/D = 52.5$.

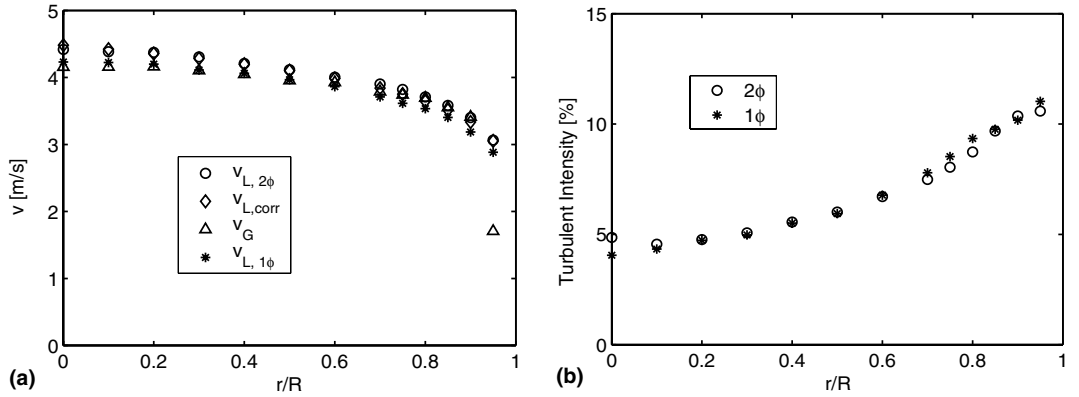

Fig. 10. Mean velocity (a) and turbulent intensity (b) profiles for Run 9 in 50.8 mm ID test section at $z/D = 52.5$.

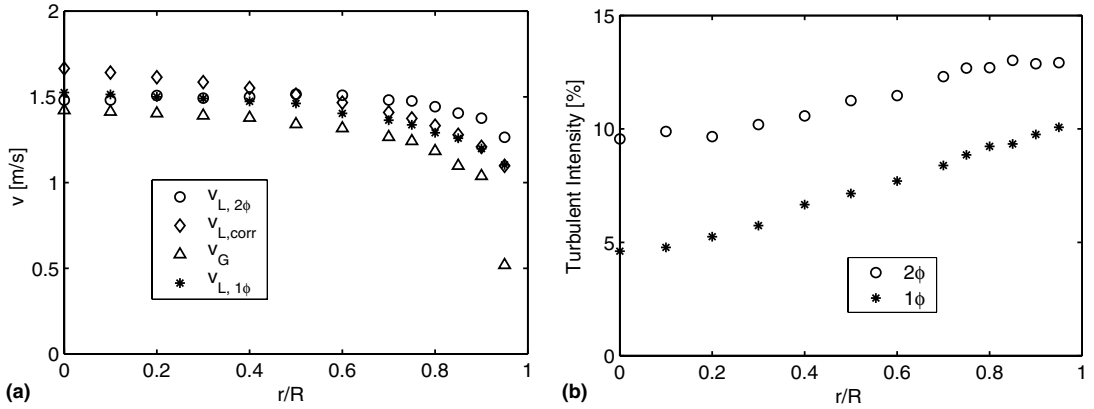

Fig. 11. Mean velocity (a) and turbulent intensity (b) profiles for Run 10 in 50.8 mm ID test section at $z/D = 52.5$.

$$
\begin{aligned}
v_{\mathrm{L}}(r) &= v_{\mathrm{L,max}}\left(1-\frac{r}{R}\right)^{\frac{1}{n}},\\
v_{\mathrm{L,max}} &= \frac{(n+1)(2n+1)}{2n^2}\,\frac{\langle j_{\mathrm{L}}\rangle}{1-\langle\epsilon\rangle},\\
n &= 2.95 Re_{\mathrm{L}}^{0.0805},\\
Re_{\mathrm{L}} &= \frac{2\rho_{\mathrm{L}}\langle j_{\mathrm{L}}\rangle R}{\eta_{\mathrm{L}}},
\end{aligned}
\tag{2}
$$

where, v_{L} is the local liquid velocity, ρ_{L} and η_{L} are the density and dynamic viscosity of the liquid phase, and $\langle\epsilon\rangle$ is the area-averaged void fraction;

(4) interpolated bubble velocity measured by the conductivity probe at locations $z/D = 34$ and 67 in 50.8 mm ID test section (v_{G}).

In each figure, sub-figure (b) shows the radial profile of the turbulence intensity measured in two-phase flows and the single-phase flows having the same superficial liquid velocity. The following observations can be made from the measurements:

(a) In general, the velocity distributions in two-phase flows had similar profiles to those in the turbulent single-phase flow. However, the presence of the bubbles flattened the liquid velocity profiles, which was also observed by Wang et al. (1987). This effect was more pronounced in the flow conditions having lower superficial liquid velocity and higher void fraction.

(b) For some flow conditions, the maximum liquid velocity occurred off the pipe center line, for example, at $r/R = 0.85$ for Run 5 and $r/R = 0.5$ for Run 10. Wang et al. (1987) and Kashinsky and Randin (1999) had similar observations in their bubbly flow experiments. As stated earlier, in downward two-phase flows, the bubbles tend to migrate to the center of the pipe, due to the action of the lift force which acts towards the center of the pipe. Furthermore, the bubbles move slower than the surrounding liquid due to the buoyancy. This leads to the formation of the wake region to the downstream side of the bubbles. The liquid velocity in the wake region is lower than that of the surrounding liquid. Hence, the slow moving bubbles in the central part of the pipe tend to reduce the liquid velocity. Thus, the mean axial velocity profiles tend to be flattened and might lead to an off-center peak in the flow conditions with higher void fraction bubbly flows. This is consistent with the observations by Kashinsky and Randin (1999) that the larger the void fraction, the greater is the possibility of this phenomenon to occur. Since the magnitude of the velocity defect in the wake region is approximately constant, this effect diminishes for the flow conditions with high superficial liquid velocity, for example Runs 8 and 9 as opposed to Runs 5 and 10 which have lower superficial liquid velocity. However, Wang et al. (1987) attributed this phenomenon to bubble "coring" in the downward flow, and argued that the liquid in the core tended to diverge into the low void fraction region near the wall.

(c) The sub-figures (b) show the turbulent intensity profiles of the two-phase flow conditions as well as the single-phase flow conditions with the same superficial liquid velocity. The comparison shows that in general, the turbulence intensity is increased by introduction of the gas phase into the flow. However, in the case of flow conditions with low void fractions (<1%),

the turbulent intensity was not significantly affected. With larger void fraction, the turbulence intensity increased, especially in the core region.

(d) It is noted that the turbulent intensity showed a local peak near $r/R = 0.8$ in Runs 5 and Run 10. Also in these flow conditions, the mean liquid velocity profile had a peak at $r/R = 0.85$ and 0.5, respectively. Indeed, the velocity profiles in these flow conditions are significantly depressed in the center and have an inflection point. This implies that there is more vorticity generation in these flow conditions. Hence, it can be speculated that these flow conditions have increased turbulence.

The addition of gas phase usually increases the turbulent intensity in continuous liquid phase. However, Serizawa et al. (1975) Tsuji and Morikawa (1982), and Wang et al. (1987) observed a reduction of the axial liquid turbulence in some two-phase flow conditions. However, in their experiments, the size of the particles of the dispersed phase was considerably smaller than that in the current experiments. In the current experiments, no significant turbulence reduction was observed.

4. Interfacial area transport

In the two-fluid model formulation, each phase is treated separately in the formulation of conservation equations (Ishii, 1975). After a proper averaging, the conservation equations for the mass, momentum and energy are written separately for each phase. Since the averaged macroscopic fields for each phase are not independent of each other, these two sets of the conservation equations are coupled through the interfacial interaction terms. The phase interaction terms can be expressed in terms of the interfacial area concentration, a_i, and the corresponding driving forces (Kocamustafaogullari and Ishii, 1995) as,

$$\text{Interfacial Transfer Term} = a_i \times \text{Driving Force}. \tag{3}$$

Therefore, a closure relation for the interfacial area concentration is needed to complete the model. Traditionally, this closure problem is solved by using flow regime-dependent experimental correlations for a_i along with the flow regime transition criteria. However, this approach does not dynamically represent the changes in the interfacial structure. Considering the drawbacks of this approach, interfacial area transport equation was proposed by Ishii (1975) and Kocamustafaogullari and Ishii (1995). The Interfacial area transport model is a dynamic approach for predicting the interfacial area concentration in two-phase flow systems, as opposed to the static, algebraic models based on the flow regime maps. The interfacial area transport equation dynamically predicts the change of the interfacial area concentration along a flow field from given boundary conditions.

The foundations of the interfacial area transport equation were first established by Kocamustafaogullari and Ishii (1995). The general form of the interfacial area transport equation is given by,

$$\frac{\partial a_i}{\partial t} + \nabla \cdot \left(a_i \vec{v}_i \right) = \frac{2}{3} \frac{a_i}{\epsilon} \left(\frac{\partial \epsilon}{\partial t} + \nabla \cdot (\epsilon \vec{v}_G) - \eta_{ph} \right) + \sum_j \phi_j + \phi_{ph}. \tag{4}$$

Here, the first term on the right hand side of the equation represents the source in the interfacial area concentration due to the change in the volume of the dispersed phase. In this term, η_{ph} is the

net rate of volume generated by nucleation and collapse of bubble due to condensation per unit mixture volume. It may be noted that $\overrightarrow{v_i}$ is the velocity of the interface, while $\overrightarrow{v_G}$ is gas phase velocity. For bubbly flow, these two velocities are approximately same. The terms ϕ_j and ϕ_{ph} represent the source and sink terms due to the bubble interaction mechanisms and phase change, respectively. In order to complete the interfacial area transport model, constitutive relations for the source and sink terms appearing on the right hand side of the interfacial area transport equation have to be developed. This is achieved by mechanistically modeling the bubble interaction mechanisms in a two-phase flow. Recently, one-group interfacial area transport equation for adiabatic air–water bubbly flows was developed for pipe and channel flows (Wu et al., 1998; Kim, 1999). Following that, two-group interfacial area transport equation applicable to cap-bubbly, slug and churn-turbulent flows was developed for various channel geometry (Sun, 2001; Fu, 2001; Smith, 2002).

In one-group transport equation, three significant bubble interaction mechanisms for group-one bubbles were modeled, namely, bubble breakup due to the impact of turbulent eddies in the continuous phase (TI), bubble coalescence due to random collision of the turbulent eddies in the continuous phase (RC), and bubble coalescence due wake entrainment of following bubble into preceding bubble (WE). Finally, the one-group interfacial area transport equation for air–water two-phase flows without phase change was given by Wu et al. (1998) and Kim (1999), in one-dimensional, steady-state form as,

$$\begin{aligned}\frac{\mathrm{d}(\langle a_i\rangle\langle\langle v_G\rangle\rangle)}{\mathrm{d}z} &= \left(\frac{2\langle a_i\rangle\langle\langle v_G\rangle\rangle}{3p}\right)\left(\frac{\mathrm{d}p}{\mathrm{d}z}\right) + C_{TI}\frac{1}{18}\left(\frac{\langle a_i\rangle^2}{\langle\epsilon\rangle}\langle u_t\rangle\right)\left(1-\frac{We_{cr}}{We}\right)^{1/2}\exp\left(-\frac{We_{cr}}{We}\right)\\ &\quad - C_{RC}\frac{1}{3\pi}\frac{\langle a_i\rangle^2\langle u_t\rangle}{\langle\epsilon\rangle_{max}^{1/3}(\langle\epsilon\rangle_{max}^{1/3}-\langle\epsilon\rangle^{1/3})}\left(1-\exp\left(-C\frac{\langle\epsilon\rangle_{max}^{1/3}\langle\epsilon\rangle^{1/3}}{\langle\epsilon\rangle_{max}^{1/3}-\langle\epsilon\rangle^{1/3}}\right)\right)\\ &\quad - C_{WE}C_D^{1/3}\frac{\langle a_i\rangle^2\langle u_t\rangle}{3\pi}. \end{aligned} \tag{5}$$

In this equation, the first term on the right hand side represents the change in the interfacial area concentration due to compressibility of the dispersed phase, while the remaining three terms represent the change in the interfacial area concentration due to impact of turbulent eddies in the continuous phase (TI), random collision of bubbles driven by the turbulent eddies in the continuous phase (RC) and coalescence of bubbles due to wake entrainment (WE) respectively. These interaction terms contain empirical coefficients, i.e. C_{TI}, C_{RC}, C, and C_{WE}, which have to be found from experimental data. In this equation, p, u_t, We and C_D are the local pressure, rms turbulent velocity fluctuation in liquid phase, particle Weber number and particle drag coefficient respectively. Furthermore, the operators $\langle\cdot\rangle$ and $\langle\langle\cdot\rangle\rangle$ represent the area averaged and void-weighted area averaged quantities respectively.

4.1. Experimental results

Figs. 12 and 13 show the axial development of the interfacial area concentration for the bubbly flow conditions. In general, it was found that the area-averaged void fraction tends to decrease in the down stream direction for flow conditions with low superficial liquid velocities ($j_L < 2.5$ m/s),

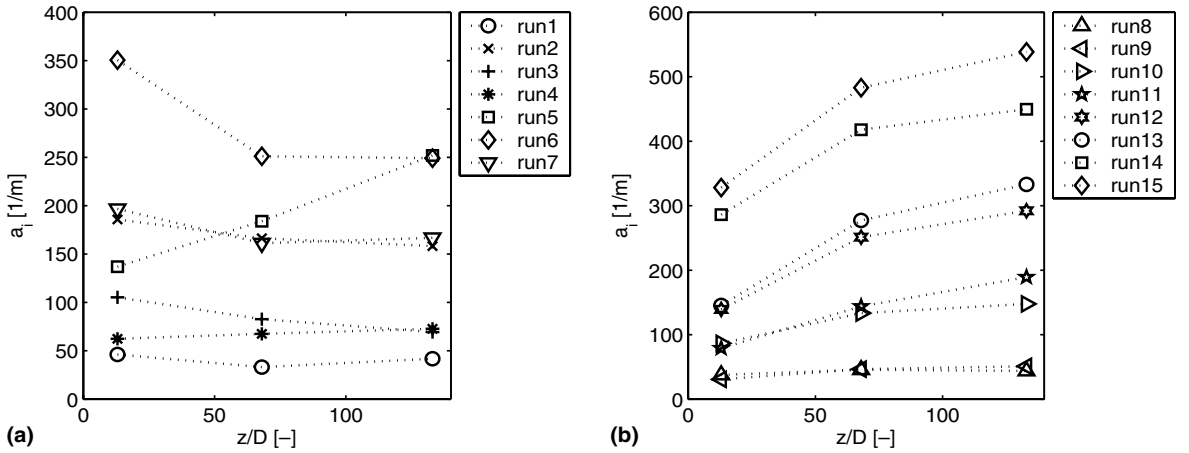

Fig. 12. Axial development of area-averaged interfacial area concentration in 25.4 mm ID test section.

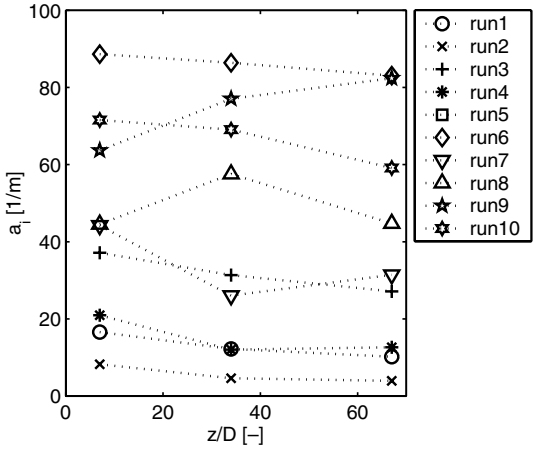

Fig. 13. Axial development of area-averaged interfacial area concentration in 50.8 mm ID test section.

while it increases in the flow conditions with higher superficial liquid velocities. Considering air as an ideal gas, void fraction and pressure are inversely proportional to each other for constant bubble velocity. In downward flow, the hydrostatic pressure increases in the downstream direction while the frictional pressure drop decreases the pressure in the downstream direction. Hence, in the case of low liquid flow rates, the pressure increases at higher z/D locations causing the void fraction to decrease, while the opposite is observed in the case of flow conditions with high liquid flow rates. Interfacial area concentration is proportional to the void fraction. Hence in most of the bubbly flow conditions, the axial development of the interfacial area concentration is similar to that of the void fraction.

Bubble coalescence mechanisms decrease the interfacial area concentration, while bubble breakup mechanisms contribute to the increase of the interfacial area concentration. For example, Runs 1, 2, and 6 in the 25.4 mm ID test section have same superficial liquid velocity

($j_L = 1.25$ m/s), but different superficial gas velocities ($j_G = 0.087$, 0.15, and 0.243 m/s, respectively). The void fraction in these flow conditions is progressively higher. It can be observed that decrease in the interfacial area concentration is more significant in Run 6 as compared to Runs 1 and 2. This is due to increased bubble coalescence. The effect of increasing the superficial liquid velocity is also evident. Runs 2, 3, and 4 in the 25.4 mm ID test section have similar superficial gas velocities ($j_G = 0.087$, 0.085, and 0.086 m/s, respectively), while different superficial liquid velocities ($j_L = 1.25$, 2.12, and 3.11 m/s respectively). It can be observed that the interfacial area concentration decreases along the flow direction for Runs 2 and 3, while increases for Run 4. This can be attributed to the breakup of the bubbles due to increased turbulence with increased liquid velocity. Runs 8, 9, 10, 11, 12, and 13 in the 25.4 mm ID test section, which have high liquid velocity also show significant increase in the interfacial area concentration along the flow direction. Similar trends are also observed in the 50.8 mm ID test section.

Runs 7 and 14 in the 25.4 mm ID test section are near the bubbly to slug transition boundary. They are, indeed, in the cap-bubbly flow regime. Figs. 14 and 15 show the axial development of the void fraction and the interfacial area concentration for group 1 and group 2 bubbles in these flow conditions. In Run 7, the void fraction of group 1 bubbles decreases while that of group 2 bubbles increases in the downstream direction. This suggests that the group 2 bubbles are formed by the coalescence of group 1 bubbles. However, Run 14 shows an opposite trend. In this flow condition, the void fraction of group 2 bubbles decreases in downstream direction, while that of group 1 bubble increases. The area-averaged interfacial area concentration profiles also show the similar trends. This indicates that the bubble breakup mechanism is significant. Run 14 has higher superficial liquid velocity ($j_L = 3.99$ m/s) as compared to Run 7 ($j_L = 2.12$ m/s). Hence, there is enhanced turbulence in these flow conditions which leads to the increase of the bubble breakup.

4.2. Model predictions

The predictions from the interfacial area transport model are compared with the experimental data from the conductivity probe. The interfacial area concentration along the test section is

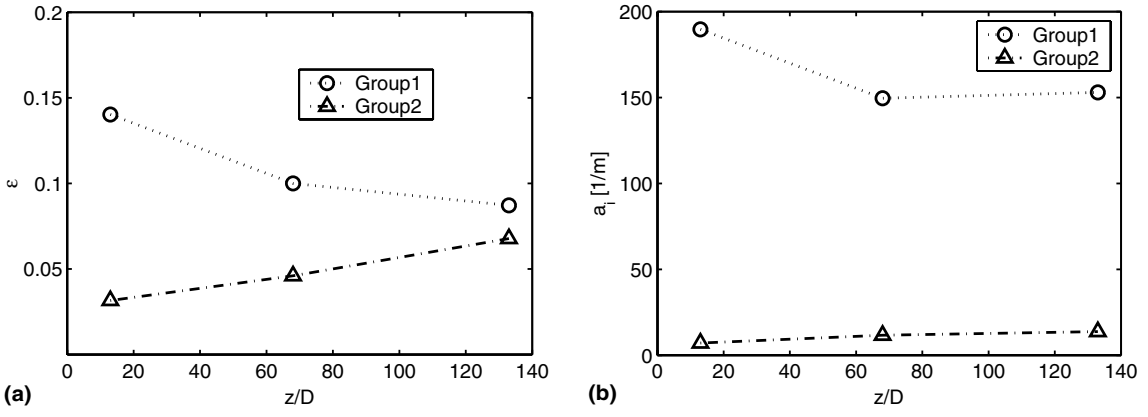

Fig. 14. Axial development of local parameter for Run 7 in 25.4 mm ID test section. (a) Void fraction; (b) interfacial area concentration.

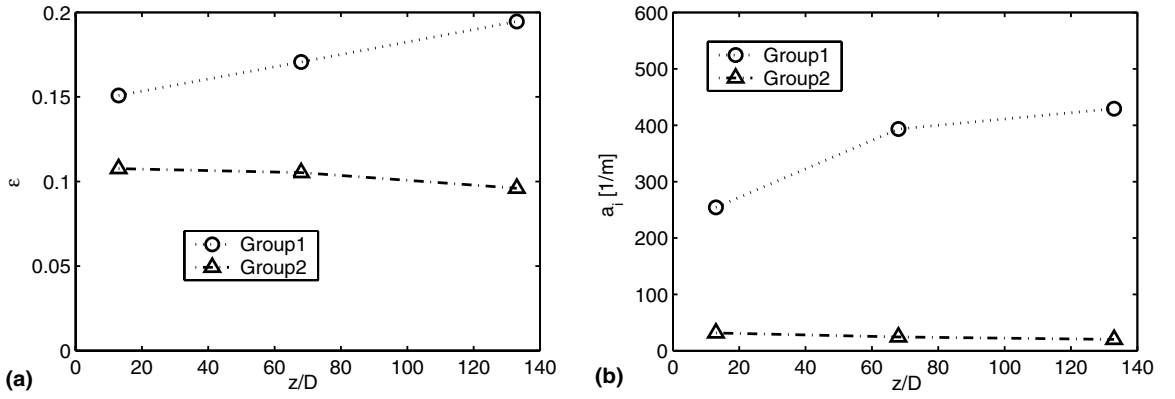

Fig. 15. Axial development of local parameter for Run 14 in 25.4 mm ID test section. (a) Void fraction; (b) interfacial area concentration.

calculated by solving Eq. (5) from the boundary conditions measured experimentally. The comparison of the area-averaged interfacial area concentration with the model are shown in Figs. 16 and 17. The error bars in the figures show ±10% of the measured value. Here, the flow conditions that had only group 1 bubbles are used for model evaluation. It was observed that the agreement between the model predictions and the measured values was within ±10% for most of the flow conditions in the 25.4 mm ID test section that did not show the existence of the group 2 bubbles. For the 50.8 mm ID test section, the model agreed well for Runs 1, 2, 3, 5, and 6. The empirical coefficients in the bubble interaction mechanisms were determined from the experimental data. It was found that only the coefficient that accounts for the rate of disintegration of the bubbles due to the impact of the turbulent eddies was changed from that in the upward flow. The coefficient was found to be 0.4 times of that for the upward flow. This may be attributed to the different

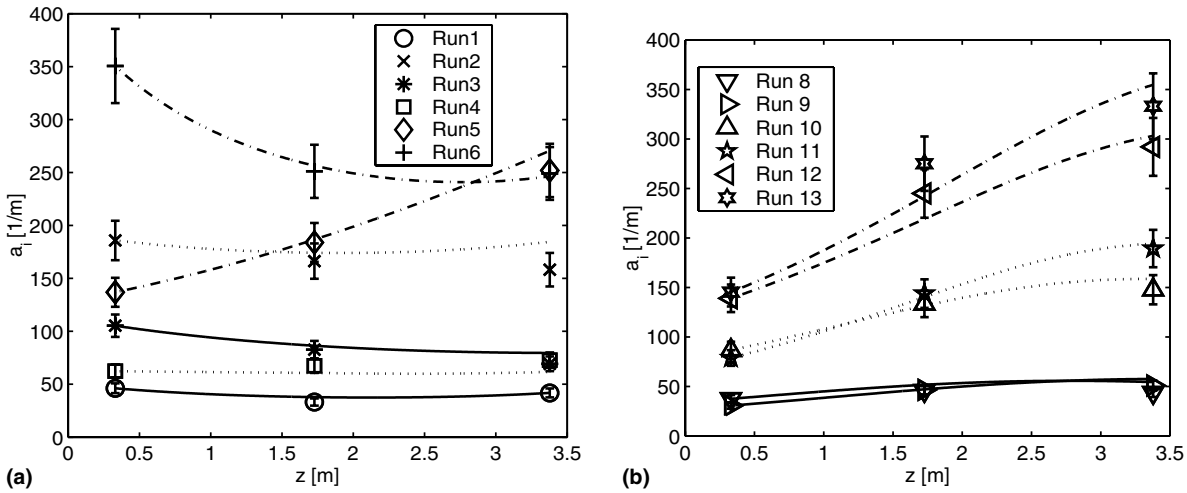

Fig. 16. Comparison of model and data for 25.4 mm ID test section.

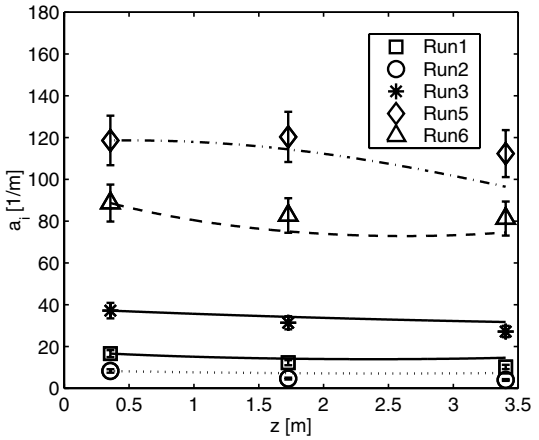

Fig. 17. Comparison of model and data for 50.8 mm ID test section.

Table 3
Coefficients in bubble interaction mechanisms

Flow direction	Bubble breakup by impact of turbulent eddies (TI)	Bubble coalescence by wake entrainment (WE)	Bubble coalescence by random collision (RC)
Upward flow	$C_{TI} = 0.085$, $We_{cr} = 6.0$	$C_{WE} = 0.002$	$C_{RC} = 0.0041$, $C = 3$, $\epsilon_{max} = 0.75$
Downward flow	$C_{TI} = 0.034$, $We_{cr} = 6.0$	$C_{WE} = 0.002$	$C_{RC} = 0.0041$, $C = 3$, $\epsilon_{max} = 0.75$

turbulence structure in the downward flow. Further investigation is needed to clearly understand this phenomenon. The values of the model coefficients used in Eq. (5) are summarized in Table 3.

It is interesting to study the relative contributions of the different mechanisms to the change in the interfacial area concentration under different boundary conditions. This study helps to understand the sensitivity of the model and that of the individual mechanisms to the different boundary conditions. Figs. 18–20 show the contribution of the individual mechanisms to the change in the interfacial area concentration for Runs 2, 9, and 6 respectively in the 25.4 mm ID test section. In addition to the three bubble interaction mechanisms, the changes in the pressure and in the gas velocity ($\langle\langle v_G \rangle\rangle$) along the test section also contribute to the change in the interfacial area concentration. In the figures, these two factors are abbreviated as PEXP and VELDIV, respectively. The sources to the interfacial area are from the expansion due to pressure change (PEXP) and the divergence of the gas velocity (VELDIV). The following observations can be made from the study of the contribution of the individual mechanisms:

(1) In all these three cases, pressure increases in the downstream direction, leading to a decrease in the void fraction and hence in the interfacial area concentration. This fact is reflected by the model predictions.

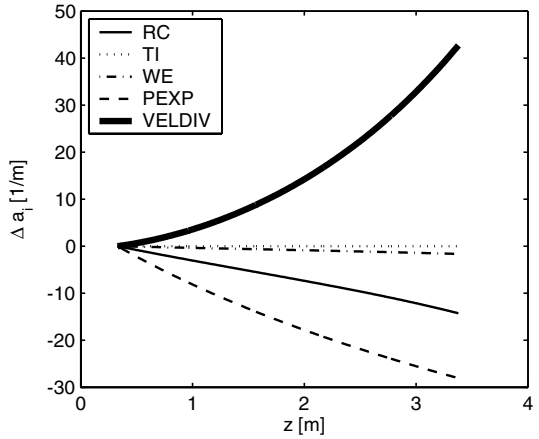

Fig. 18. Contribution of individual mechanisms to the change in interfacial area concentration for Run 2 in 25.4 mm ID test section.

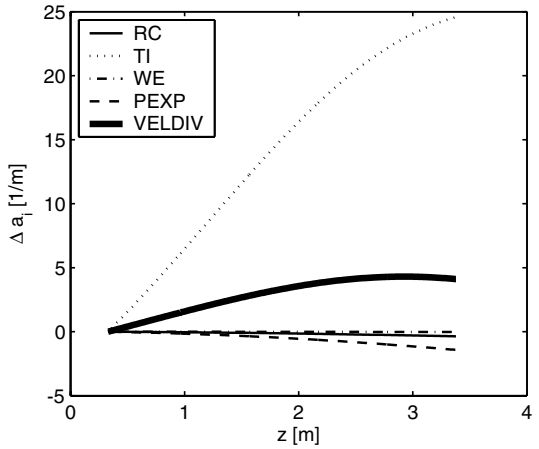

Fig. 19. Contribution of individual mechanisms to the change in interfacial area concentration for Run 9 in 25.4 mm ID test section.

(2) The change in the void-weighted gas velocity had significant impact on the change in the interfacial area concentration. Decreasing void-weighted gas velocity tends to increase the interfacial area concentration. In Runs 2 and 9, there was an increase in the interfacial area change due to the velocity decrease, while in the case of Run 6, there was a decrease up to $z/D = 67$ and then an increase to $z/D = 133$. This may be due to the change in the axial derivative of the void-weighted gas velocity because of formation of bigger bubbles in the case of Run 6, which is near the bubbly-to-slug transition region.

(3) Runs 2 and 6, which are low superficial liquid velocity conditions ($j_L = 1.245$ m/s), did not show any contribution from the mechanisms of disintegration of bubbles due to TI. This is due to low liquid phase turbulence in those flow conditions. On the other hand, Run 9, which

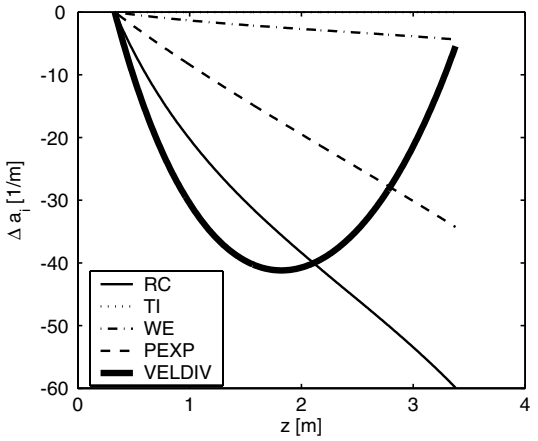

Fig. 20. Contribution of individual mechanisms to the change in interfacial area concentration for Run 6 in 25.4 mm ID test section.

is a high superficial liquid velocity condition ($j_L = 5.07$ m/s), showed a significant contribution from the TI mechanism.

(4) Coalescence of bubbles due to RC was a dominant mode in the low superficial liquid velocity conditions, i.e., Runs 2 and 6. Out of these two, Run 6 is the condition with relatively higher void fraction ($\epsilon = 0.191$), which clearly showed higher rate of RC as compared to Run 2 ($\epsilon = 0.067$), as anticipated.

(5) In general, the bubble coalescence due to WE had small contribution to the change in the interfacial area concentration. However, Run 6 which had comparatively higher void fraction as compared to the other flow conditions, showed higher contribution from WE as compared to the other two flow conditions. It is interesting to note that the larger the bubble diameter the higher is the contribution of WE. Indeed, the average bubble diameter in Run 6 ($D_{Sm} = 3.6$ mm) was higher compared to other two flow conditions (2 and 1.6 mm for Runs 2 and 9, respectively), since Run 6 is near the bubbly-to-slug transition boundary.

5. Conclusions

The present research performed detailed experimental studies in vertical co-current air–water downward two-phase flow. A less subjective method was employed in the flow regime identification study by using an impedance void meter coupled with a self-organized neural network. In the experiment, detailed local two-phase flow parameters were acquired by a conductivity probe and LDA. The local parameter measurements revealed the details of the interfacial structures in the downward two-phase flow, while the area-averaged parameters at the three axial locations revealed the axial development of the two-phase flow parameters, and hence the bubble interaction mechanisms. The effect of the boundary conditions on the bubble interaction mechanisms was also evident from this study. Interfacial area transport model for adiabatic air–water two-phase flow was evaluated with the area-averaged data obtained from the experiments.

In summary, following observations can be made from the present study.

(1) The flow regime map for downward flow showed quite different characteristic from upward flow. Especially, the existence of the kinematic shock condition at the boundary between the bubbly and annular flows is a unique feature. This abrupt transition from the bubbly to annular flows was observed in the 50.8 mm ID test section. This phenomenon was not observed in the 25.4 mm ID test section in the current span of the flow conditions.
(2) The flow regime maps for the two test sections were quite different. This showed that there was a significant impact of the test section size on the flow regime map in case of downward flow.
(3) Center peaked void distribution profiles were observed in most of the bubbly flow conditions. This is consistent with the direction of the lift force, which acts on the bubbles towards the center line of the test section in the case of downward flow. However, the off-center peaked void profile for some of the bubbly flow conditions needs further investigation.
(4) The center peaking was more pronounced with increasing superficial liquid flow rate. The test section diameter also had some impact on the void profiles. The void profiles in the 50.8 mm ID test section were flatter as compared to those in the 25.4 mm ID test section.
(5) In the downward flow, the bubbles move slower than the surrounding liquid. This can be explained based on the directions of the buoyancy and drag forces acting on the bubbles.
(6) In most of the flow conditions, the area-averaged void fraction tended to decrease in downstream direction due to in crease in the hydrostatic pressure.
(7) Increase in the superficial liquid flow rate increased the turbulence and hence the bubble disintegration due to the impact of turbulent eddies. On the other hand, bubble coalescence was dominated in the flow conditions with low superficial liquid velocities.
(8) In most of the bubbly flow conditions, the one-group interfacial area transport model worked reasonably well. The evaluation results showed that the turbulent impact coefficient which accounts for the rate of the bubble disintegration due to the impact of turbulent eddies in the liquid phase had to be decreased from that in the upward flow. Since turbulence in a two-phase flow system is a combination of bubble-induced and wall-induced turbulence, the center-peak void profile in downward flow creates a different turbulent structure than that in most of the upward flows. This has an impact on the interaction of turbulent eddies with bubbles. The empirical coefficients accounting for the other mechanisms were found to be the same compared to the upward flow. The model predictions were within $\pm 10\%$ for most of the bubbly flow conditions in the 25.4 mm ID test section. The agreement was not as good as in the flow conditions in the 50.8 mm ID test section. Nevertheless, the overall results were quite encouraging.

References

Barnea, D., 1987. A unified model for predicting flow pattern transitions for the whole range of pipe inclinations. Int. J. Multiphase Flow 13, 1–12.

Barnea, D., Shoham, O., Taitel, Y., 1982. Flow pattern transition for vertical downward two-phase flow. Chem. Eng. Sci. 37, 741–744.

Crawford, T.J., Weinberger, C.B., Weisman, J., 1985. Two-phase flow patterns and void fractions in downward flow. Part i: Steady-state flow patterns. Int. J. Multiphase Flow 11, 761–782.

Durst, F., Zare, M., 1975. Laser Doppler measurements in two-phase flows. In: Proc. of the LDA Symposium, Copenhagen, pp. 403–429.

Fu, X.Y., 2001. Interfacial Area Measurement and Transport Modeling in Air–Water Two-phase Flow. Ph.D. thesis, Purdue University, West Lafayette, IN, USA.

Goda, H., 2001. Flow Regimes and Local Parameter Measurements for Downward Two-phase Flow. Master's thesis, Purdue University, West Lafayette, IN, USA.

Hibiki, T., Hogsett, S., Ishii, M., 1998. Local measurement of interfacial area, interfacial velocity and liquid turbulence in two-phase flow. Nucl. Eng. Design 184, 305–318.

Ishii, M., 1975. Thermo-fluid Dynamic Theory of Two-phase Flow. Eyrolles Paris: Scientific and Medical Publication of France, Paris.

Ishii, M., Zuber, N., 1979. Drag coefficient and relative velocity in bubbly, droplet or particulate flows. AIChE J. 25, 843–855.

Kashinsky, O.N., Randin, V.V., 1999. Downward bubbly gas–liquid flow in a vertical pipe. Int. J. Multiphase Flow 25, 109–138.

Kawaji, M., Ng, Y.S., Banerjee, S., Yadigaroglu, G., 1985. Reflooding with steady and oscillatory injection. I. Flow regimes, void fraction heat transfer. J. Heat Transfer—Trans. ASME 107, 670–678.

Kim, S., 1999. Interfacial Area Transport Equation and Measurement of Local Interfacial Characteristics. Ph.D. thesis, Purdue University, West Lafayette, IN, USA.

Kim, S., Fu, X.Y., Wang, X., Ishii, M., 2000a. Development of the miniaturized four-sensor conductivity probe and the signal processing scheme. Int. J. Heat Mass Transfer 43, 4101–4118.

Kim, S., Fu, X.Y., Wang, X., Ishii, M., 2000b. Development of the miniaturized four-sensor conductivity probe and the signal processing scheme. Int. J. Heat Mass Transfer 43, 4101–4118.

Kocamustafaogullari, G., Ishii, M., 1995. Foundations of interfacial area transport equation and its closure relations. Int. J. Heat Mass Transfer 38, 481–493.

Marie, J.L., Lance, M., 1983. Turbulence measurements in two-phase bubbly flows using laser Doppler anemometry. In: Delhaye, J.M., Cognet, G. (Eds.), Measuring Techniques in Gas–Liquid Two-phase Flow. Springer, New York, pp. 141–148.

Mi, Y., Ishii, M., Tsoukalas, L.H., 2001. Flow regime identification methodology with neural networks and two-phase flow models. Nucl. Eng. Design 204, 87–100.

Mishima, K., Ishii, M., 1984. Flow regime transition criteria for upward two-phase flow in vertical tubes. Int. J. Heat Mass Transfer 27, 723–737.

Ohba, K., Yuhara, T., Matsuyama, H., 1986. Simultaneous measurements of bubble and liquid velocities in two-phase bubbly flow using Laser Doppler Velocimeter. Bull. JSME 29, 2487–2493.

Oshinowo, T., Charles, M.E., 1974. Vertical two-phase flow. Part I. Flow pattern correlation. Can. J. Chem. Eng. 52, 25–35.

Paranjape, S.S., 2003. Local Parameter Measurements and Interfacial Area Transport in Downward Two-phase Flow. Master's thesis, Purdue University, West Lafayette, IN, USA.

Revankar, S.T., Ishii, M., 1993. Theory and measurement of local interfacial area using a four-sensor probe in two-phase flow. Int. J. Heat Mass Transfer 36, 2997–3007.

Serizawa, A., Kataoka, I., Michiyoshi, I., 1975. Turbulence structure of air–water bubbly flow-I, II and III. Int. J. Multiphase Flow 2, 221–259.

Smith, T.R., 2002. Two-group Interfacial Area Transport Equation in Large Diameter Pipes. Ph.D. thesis, Purdue University, West Lafayette, IN, USA.

Sun, X., 2001. Two-group Interfacial Area Transport Equation for a Confined Test Section. Ph.D. thesis, Purdue University, West Lafayette, IN, USA.

Taitel, Y., Barnea, D., 1983. Counter current gas–liquid vertical flow, model for flow pattern and pressure drop. Int. J. Multiphase Flow 9, 637–647.

Taitel, Y., Bornea, D., Duckler, A.E., 1980. Modelling flow pattern transitions for steady upward gas–liquid flow in vertical tubes. AIChE J. 26, 345–354.

Theofanous, T.G., Sullivan, J.P., 1982. Turbulence in two-phase dispersed flows. J. Fluid Mech. 116, 343.

Tsuji, Y., Morikawa, Y., 1982. LDV measurement of an air–solid two-phase flow in a horizontal pipe. J. Fluid Mech. 120, 385–409.

Usui, K., Sato, K., 1989. Vertically downward two-phase flow. (I) Void distribution and average void fraction. J. Nucl. Sci. Technol. 26, 670–680.

Velidandla, V., Putta, S., Roy, R.P., 1996. Velocity field in isothermal turbulent gas–liquid flow through a pipe. Exp. Fluids 21, 347–356.

Wang, S.K., Lee, S.J., Jones, O.C.J., Lahey, R.T.J., 1987. 3-D Turbulence structure and phase distribution measurements in bubbly two-phase flows. Int. J. Multiphase Flow, 13.

Wu, Q., Ishii, M., 1999. Sensitivity study on double sensor conductivity probe for the measurement of interfacial area concentration in bubbly flow. Int. J. Multiphase Flow 25, 155–173.

Wu, Q., Kim, S., Ishii, M., Beus, S.G., 1998. One-group interfacial area transport in vertical bubbly flow. Int. J. Heat Mass Transfer 41, 1103–1112.

Yadigaroglu, G., 1983. Flow regimes and carryover during reflooding. Trans. Am. Nucl. Soc. 45, 455–456.

Yamaguchi, K., Yamazaki, Y., 1984. Combined flow pattern map for cocurrent and countercurrent air–water flows in vertical tube. J. Nucl. Sci. Technol. 21, 321–327.